Signal Decomposition with InSAR Displacement Time Series Above a Storage Cavern Field: Example Epe (NRW, Germany)

Alison Seidel, Malte Westerhaus, Markus Even, and Hansjörg Kutterer

Abstract

Time series of interferometric SAR (InSAR) images offer the potential to detect and monitor surface deformation with high spatial resolution, even for slow deformation processes. However, many different sources contribute to phase changes which are used in InSAR to estimate displacements. Complex displacement mechanisms or strong atmospheric contributions can complicate the separation of these contributions and even cause problems when unwrapping the phase. A preliminary model of expected displacements can support this process but requires information about all involved deformation processes. However, as these processes are often the main subject of the investigation, they are not sufficiently understood in advance.

In this contribution, we approach this issue by analyzing InSAR time series results of regions with complex deformation behavior with the established statistical methods of principal and independent component analysis to identify dominant displacement patterns. We study Sentinel-1 InSAR data from 2015 to 2022 above the storage cavern field Epe in North Rhine Westphalia, Germany. Epe displays a spatially and temporally complex surface deformation field, which was described in previous studies as consisting of a linear signal relating to the cavern convergence as well as of seasonal and cavern pressure-dependent contributions. Our resulting displacement components can be clearly separated and appointed to different sources. This is supported by ground truth data and supplemental measurements of cavern pressure levels and groundwater levels. We also find that the previously described linear parametrization of displacements related to cavern convergence is no longer sufficient for longer time series.

Our results show that we can obtain source-dependent displacement models from long and complex InSAR time series when using ICA. These can then either be used to refine time series processing or to describe the physical processes causing to the surface displacements with a geophysical source model. Both will be the subject of future investigations.

Keywords

Component analysis · Distributed scatterers · Gas storage caverns · InSAR · Persistent scatterers · Radar interferometry · Satellite geodesy · Signal decomposition · Surface displacements

A. Seidel (✉) · M. Westerhaus · M. Even · H. Kutterer
Karlsruhe Institute of Technology, Karlsruhe, Germany
e-mail: alison.seidel@kit.edu

J. T. Freymueller, L. Sánchez (eds.), *Together Again for Geodesy*,
International Association of Geodesy Symposia 157, https://doi.org/10.1007/1345_2025_284

1 Introduction

Time series of the satellite-based imaging method of interferometric SAR (InSAR) can be used to detect and monitor surface displacements efficiently. InSAR utilizes the reflection of radar waves on the ground and measures the change of phase of the wave between two acquisitions to determine surface displacements along the line of sight (LOS) of the satellite in magnitudes of millimeters. Thus, InSAR complements the better-established methods of GNSS and leveling measurements. While GNSS provides 3D displacements with high temporal resolution, at usually very sparsely distributed stations, and leveling can measure vertical displacements on a denser spatial resolution than GNSS, but with measurements often once per year or even rarer, InSAR observes displacements both frequently and spatially densely.

However, other spatially correlated signals, especially atmospheric contributions can often not be removed completely from InSAR results. Moreover, rapid changes in surface displacements can also lead to parts of the displacements being falsely identified as spatially correlated noise (scn). Consequently, they are removed from the final displacement result as shown by Even et al. (2020). Even if the atmospheric contributions can be sufficiently modeled with high spatial and temporal coverage, multiple displacement phenomena will remain which need to be separated. Although the respective causes might neither be connected nor be of particular interest, they will have impact on the analysis results as they superpose each other. This can complicate the interpretation of the displacement map.

If knowledge about the respective local displacement processes is available, individual time series can be analyzed manually as a first option. Then, only such scatterers are selected that exclusively contain the desired signal. However, this can lead to a loss of information in scatterers that contain multiple signals contributions.

If a deformation process is sufficiently understood, it is – as a second option – also possible to make predictions for future displacements that follow this process and to detect unexpected changes in surface behavior quickly. Subsequently, one can then deduce if the effect could relate to the source of interest or if it is caused by other processes such as surface response to precipitation. Thus, it is important to be able to differentiate displacements from different superposing source mechanisms.

Here, we analyze InSAR time series with statistical component analysis methods to separate the different signals in a complex displacement field statistically. By this, we explore a method to obtain displacements originating from individual sources from complex conditions without prior knowledge.

Our study area is the gas storage cavern field Epe where Even et al. (2020, 2022) described a complex surface displacement field with a 3-year InSAR time series study. We utilize their method for joint processing of Persistent and Distributed Scatterers (PS and DS) for a longer, 7-year time series and examine these results with the component analyses. In doing so, we gain a deeper understanding of the source processes of the surface displacements, and we can show that the components can provide a better displacement model than the parametrization used by Even et al. (2020, 2022).

2 Area of Study: Epe Gas Cavern Field

2.1 Overview

The gas storage cavern field Epe in NRW, Germany currently has 114 caverns located in the Zechstein salt layer in depths between 1,000 and 1,200 m which are used for brine production, oil and gas storage. More than 50 caverns, primarily located in the central and eastern part of the field (see Fig. 1), are filled with natural gas and are operated by six different gas provider companies. The companies operate the storage independently from each other, but do follow a similar cycle of filling the caverns in summer and emptying them in winter.

The cavern field is regularly monitored with annual leveling campaigns that cover over 500 measurement points across the entire field and three GNSS stations that were installed in 2018 (see Fig. 1). There are also several groundwater measurement points (GWMPs) available where water levels are measured regularly. Cavern filling levels are published online at the Aggregated Gas Storage Inventory (AGSI) as daily mean values for each provider since 2016 (longer for some providers). Due to these ground truth measurements and supplemental data, this region is ideal to explore and validate data-driven ways to differentiate complex displacements from different sources and obtain models, as results and predictions can be verified.

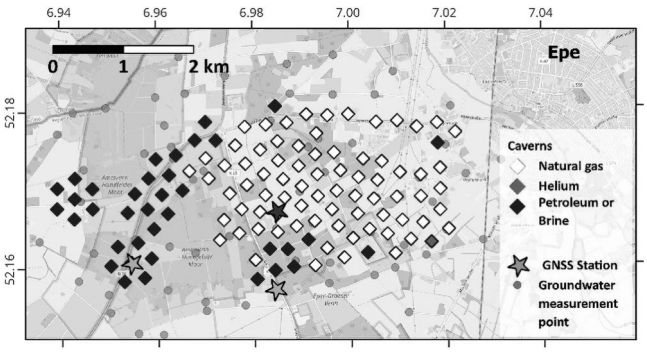

Fig. 1 Overview of the gas storage cavern field Epe. White diamonds indicate the location of natural gas caverns; black diamonds indicate liquid filled caverns

2.2 Surface Displacements and Known Sources

Convergence of gas caverns in salt bodies is a well-known process that occurs due to the lower pressure of the gas inside the caverns compared to the surrounding rock. This process usually causes a subsidence bowl in the area above the caverns which has been described at a number of places (e.g., Tajduś et al. 2021; Xie et al. 2018; Wang et al. 2014). For Epe and InSAR, Even et al. (2020, 2022) were able to develop a simple geophysical source model from 3 years InSAR time series for describing the mean subsidence rate through cavern convergence. They also observed and modeled a cyclic signal corresponding to the withdrawal and filling of the caverns. Finally, they found a strong seasonal signal superposing the other two effects. This occurs mainly in the western part of the cavern field above a fen, related to ground water levels. With the aid of groundwater measurements and the cavern filling levels, Even et al. (2020) could separate and model three main signals in the InSAR time series and described them as follows (Figs. 2 and 3):

1. An approximately linear subsidence above all caverns. The extent depends mainly on the cavern filling type.

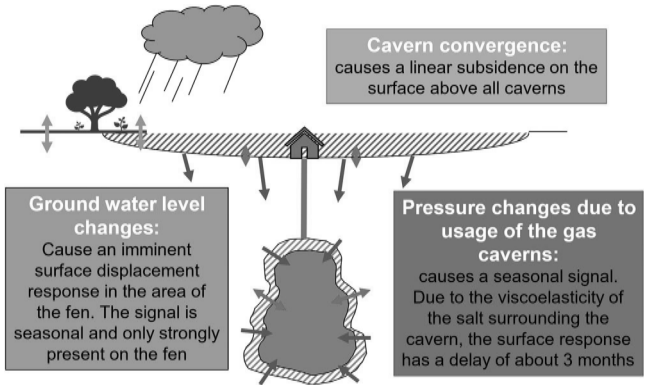

Fig. 2 Schematic depiction of the three main processes that cause surface displacements in Epe at the example of a single gas cavern

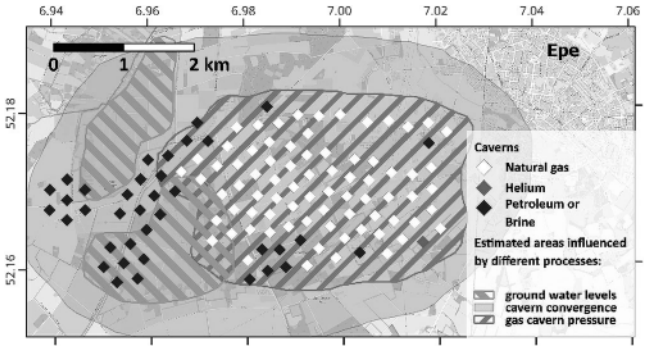

Fig. 3 Approximate areas that are affected by the different signals, derived from the results of Even et al. (2020)

2. Cyclic displacements which are a delayed response (approx. 90 days) to the withdrawal and filling of the gas caverns only.
3. A seasonal, periodic displacement over the fen area as a surface response to ground water changes.

They also parameterized the composition of the displacement field by the following equation, defining three spatially varying parameters p for the three different source mechanisms:

$$d_{\mathrm{Epe}} = a + p_{\mathrm{lin}}\, t + p_{\mathrm{pres}}\, m_{\mathrm{pres}}(t) + p_{\mathrm{fen}}\, m_{\mathrm{fen}}(t) \quad (1)$$

with d_{Epe} being the observed displacements at an arbitrary position in the cavern field, $a + p_{\mathrm{lin}}\, t$ describing the linear trend of displacements, $m_{\mathrm{pres}}(t)$ the time-dependent model curve describing the surface response due to pressure changes and $m_{\mathrm{fen}}(t)$ the time-dependent model curve for groundwater caused displacements in the fen.

2.3 Data

For this study, we processed long time series from April 2015 to December 2022 of Sentinel-1 SAR acquisitions of the two tracks ascending 15 and descending 139. Both tracks cover the complete area of interest so that we obtained time series of the respective displacements in line of sight (LOS) of both satellite view geometries. Orbit combination is only performed in one specific case, and all other analysis is done on the LOS-data. We performed our analysis on the processed tracks of both orbits separately. They generally show the same described phenomena and are in good agreement with supplemental measurements.

3 Methodology

3.1 Procedure Overview

To obtain the InSAR time series, we use an augmented version of the Stanford Method for Persistent Scatterers (StaMPS). This augmentation was developed by Even (2019) to include the selection and joint processing of Distributed Scatterers, similar to the SqueeSAR algorithm by Ferretti et al. (2011). We follow the processing settings specified in Even et al. (2020), except that we only use a simple linear model for aiding the estimation of spatially correlated noise and unwrapping. This is to simulate processing time series without having prior knowledge of the involved displacement processes. Even in these complex displacement conditions, this proved to be sufficient for the resulting displacement time series to not contain major unwrapping errors. We intentionally keep the estimated scn-phase contributions in our

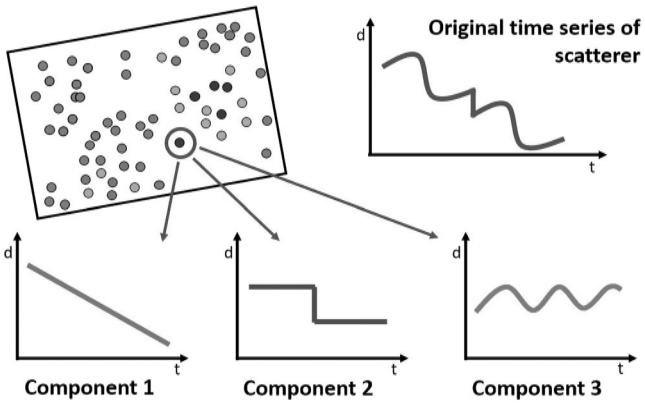

Fig. 4 Schematic depiction of three component time series that were obtained from the inverted components of a single scatterer. As comparison, the original time series is also depicted

final StaMPS result to preserve potentially leaked displacement contributions and only remove the estimated orbital error and spatially correlated look angle error contributions.

In the following, Principal Component Analysis (PCA) is applied first to our displacement time series result and then Independent Component Analysis (ICA). Other studies that utilize PCA or ICA in the InSAR context (see, e.g., Ebmeier 2016; Gaddes et al. 2018; Lin et al. 2010; Vajedian 2020) perform this kind of analysis on whole unwrapped interferograms, often in an SBAS network to keep temporal decorrelation low. Although this has the benefit of retaining the full interferograms for the analysis, this is not applicable in Epe where the displacements are small and noisy. For this reason, decorrelation in interferograms with long temporal baselines is high due to large areas of vegetation and unwrapping the interferograms individually was not successful.

As the component analysis methods reduce the dimensions of our data, we invert the obtained independent components individually back to the original spatiotemporal dimension space to obtain time series of the components (in the following called "component time series") for each scatterer (see Fig. 4). This process will be further explained in Sect. 3.3.

We can now analyze the temporal curves of the components as well as the spatial distribution and magnitude of contribution of every component in each scatterer. After we have successfully identified components that correspond to our expected source mechanisms, we use them as displacement model curves in a second InSAR time series processing to improve our result.

3.2 Principal Component Analysis

Principal component analysis (PCA) is commonly used in various scientific fields to reduce multidimensional datasets to the most relevant dimensions. It is a linear transformation which transforms the data into a new coordinate system, so that the dimension of the greatest variation in the data is used as the first principal component (PC). Accordingly, the second PC describes the dimension with second greatest variance, etc. All PCs are mutually orthogonal. PCA has been used in InSAR data analysis before: to filter out uncorrelated signals, and to differentiate signals from various sources (see, e.g., Lin et al. 2010). We perform PCA on our first result of InSAR displacement time series, where we use all time series of all scatterers of one track as input, with each SAR image acquisition time acting as individual measurement for each scatterer. Thus, we obtain PCs that describe a specific displacement behavior over the observation time, with a parameter value that describes the magnitude of this behavior in each scatterer (see Sect. 4.2, Figs. 8 and 9 for visualization). Ideally, such an analysis would result in individual components for each displacement source, as well as one for the scn term, consisting mainly of the atmospheric contributions.

We found for Epe that the first three PCs explain about 80% of the total variance in the data in both tracks. Most of the residual signal (not described by the first three PCs) is located in the area of the fen where the displacement is dominated by the surface response to ground water level changes. Here, we can expect a more complex deformation pattern that might be related to different soils and fields. Since further components show very low but overall similar magnitudes of total variance contributions, we disregard all but the first three PCs.

3.3 Independent Component Analysis

Since PCA proved to be not sufficient in differentiating the signals to separate source mechanisms (see Sect. 3.2), we use the blind source separation method Independent Component Analysis (ICA). ICA aims to describe a signal as linear mixture of various statistically independent sources or components that each has a non-Gaussian probability distribution (Comon 1994; Hyvärinen and Oja 1997). For InSAR, we assume that each time series of any individual scatterer is a mixture of signals of an arbitrary number of sources that cause a different kind of phase signal. The source and mixture relation is then described as follows (after Hyvärinen and Oja 1997):

$$x\,(t,n) = A\,(m,t)\;s\,(n,m) \tag{2}$$

where $x(t,n)$ is the matrix of observed signals, with each column representing the time series of t phase values for each of the n scatterers. Matrix $s(n,m)$ consists of m unknown independent source components (ICs) at each of the n scatterers. $A(m,t)$ then, is the unknown mixing matrix that contains

coefficients that describe the temporal behavior for each of the m components.

$$s\,(n,m) = W\,(m,t)\;\; x\,(t,n) \tag{3}$$

As $A(m,t)$ is unknown, we use its inverse $W(m,t)$, the so-called unmixing-matrix, as in Eq. (3), to transform the observation vectors to their independent sources, by maximizing the non-Gaussianity of the presumed sources. We use an implementation of the FastICA algorithm (Hyvärinen and Oja 2000) which starts with centering and whitening the data, while removing each observed signals mean value and ensuring that the signal consists of uncorrelated variables. Due to this, the order and sign of the resulting components are no longer significant. As Ebmeier (2016) describes in detail, ICA can be applied to multitemporal InSAR in two ways: by maximizing either spatial or temporal independence of the sources. We use the former approach, by treating each phase value at each SAR image acquisition time as individual observation for each scatterer, as detailed in Eq. (2). The algorithm then solves for A and s, so that the rows of A contain the "model time series" of the independent sources and s contains parameters (ICs), that describe the magnitude of how much each of these "model time series" describes the signal in each scatterer.

We can invert the ICs back individually by multiplication of $W(m,t)$ with $s(n,m)$, and setting all rows of $s(n,m)$ to zero, except the one corresponding to the desired component, and then reverse whitening and centering. Thus, we obtain component time series in the original space and time dimensions.

In general, the optimum number of ICs is unknown. Ebmeier (2016) suggests as many components as there are interferograms. However, we perform ICA on selected scatterers of a time series analysis result, which were already cleaned from most non-displacement phase contributions, rather than on whole interferograms. The exception to this might be atmospheric contributions that were not already removed through PCA. Still, we do expect that our data is mainly a mixture of different displacement sources and thus we can reduce the number of components significantly. Also, since PCA showed that only three principal components describe most of our data, we found that only two independent components already gave good results.

3.4 Parameter Fit and Reprocessing

For obtaining even more information about the spatial distribution of the signal of our displacement processes and improving our time series results, we perform a second StaMPS processing, with the same set up and data as before, but we now use our component time series as models for the displacements of the different parameters instead of a linear model. The application of this model during processing is given in Even et al. (2020). We follow the parametrization for Epe's displacement composition as described in Eq. (1) and use the normalized component time series of our two independent components as model curves for $m_{\mathrm{pres}}(t)$ and $m_{\mathrm{fen}}(t)$, respectively. Since both ICs still contain a negative trend, we fit a linear trend to them and remove it from the curves. Thus, we can fit all three parameters (p_{lin}, p_{pres}, and p_{fen}) from Eq. (1) individually to the InSAR time series through a parameter space search. We deliberately choose a lower temporal phase coherence threshold for the DS (see Even et al. 2020) to obtain a higher number of scatterers. So, the signal parts described with our models are estimated even for less-trusted scatterers.

4 Results

4.1 InSAR Displacement Field

The results of the original processing of the ascending and descending tracks, as can be seen in Fig. 5, show strong negative displacements (i.e., subsidence) in the center of the cavern field with displacements of up to 20 cm over the 7½ years of the time series. The maximum of the displacements seems to be located more to the west in the ascending than in the descending track, which indicates the presence of significant horizontal displacements. In the area of the fen, the displacements look more similar between ascending and descending.

Time series of scatterers in the fen show a negative trend that is superposed by a distinct seasonal sinusoidal signal (see Fig. 6, top). Scatterers located above the gas caverns display an even stronger negative trend, but also show cyclic behavior. In all scatterers above the gas caverns, there is a prominent negative displacement in a short period of time in 2018, while a similarly (but later reverting) strong negative displacement appears in the scatterer in the fen.

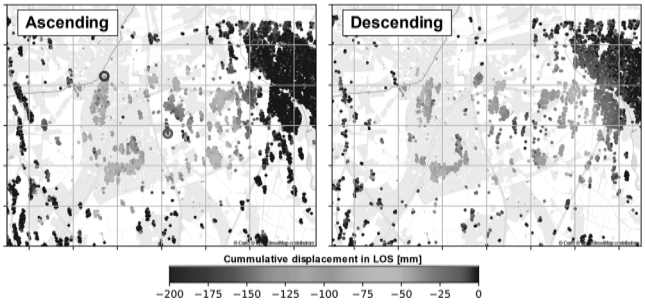

Fig. 5 Displacement field in line of sight, cumulative displacement of ascending (left) and descending (right) tracks. Two scatterer positions are marked in the left plot, of which we display time series in Fig. 6

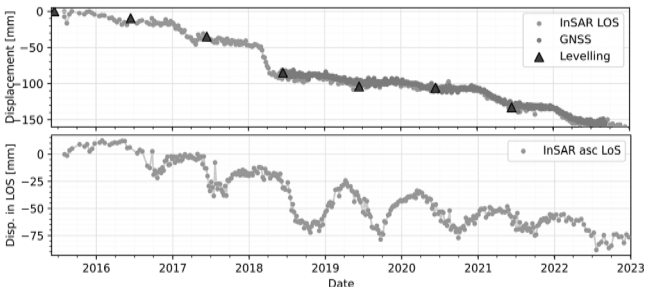

Fig. 6 InSAR time series of two scatterers of the ascending track. Both scatterers were chosen so that they are most likely only affected by the convergence caused subsidence and either the ground water-dependent displacement in the cavern pressure-dependent displacement (top) or in the fen (bottom). Both are marked in Fig. 5. Time series of GNSS station data and yearly leveling measurements (projected to LOS), located close to the first scatterer, agree with the InSAR result

However, this rapid displacement occurs in March 2018 above the gas caverns, and 3–6 months later in the fen, implying that even though appearing similar, the causes for these displacements are not likely to be the same. We validate our displacement time series, by transforming GNSS and leveling measurements at similar positions to scatterers to LOS and find a good agreement between the results (see Fig. 6, top).

4.2 Components from PCA and ICA

4.2.1 PCA

As mentioned before, the PCA shows that most of the displacement time series data can be described by three principal components. When displaying their magnitudes corresponding to each scatterer spatially (see Fig. 7), one can

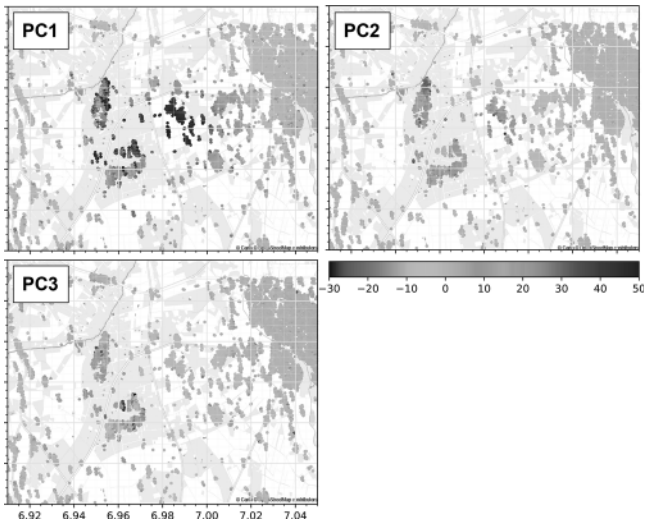

Fig. 7 Results of the PCA of the ascending track with three PCs

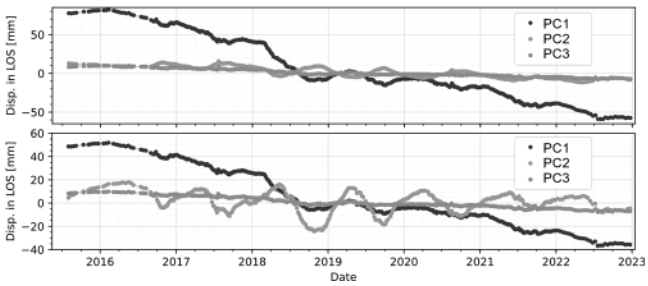

Fig. 8 Component time series of the two scatterers of the ascending track from the first three PCs. Top: in the center area of the gas caverns, bottom: in the upper fen area

see that the first PC contains a signal which is present in the entire cavern field, including the fen, having its maximum in the center of the field. Outside of the cavern field, it shows slightly negative values. The second PC has a maximum in the fen and a minimum of a similar magnitude but with a reversed sign above the gas caverns. The third PC shows a patchy behavior and is mostly present in the lower fen area.

After inverting each component individually back to the original dimension space, we can plot the component time series at the individual scatterers, as seen in Fig. 8. We show two component time series of the same scatterers as in Fig. 6, as examples, where we expect the pressure-related surface response, and respectively the ground water-dependent surface response to dominate. We see that the second PC, which is relevant in both chosen scatterers, as shown in Fig. 7, displays a periodic, seemingly seasonal behavior. Now, the first component shows a rather linear trend, but also has a cyclic component, which is inverse to PC2 at the gas caverns.

4.2.2 ICA

When trying to determine the optimum number of ICs, we find that we obtain the best results with two ICs. As the resulting components can differ when performing ICA on the same dataset multiple times, we choose those two components that statistically occurred most often. In both InSAR tracks, one of the two components only affects scatterers in the fen, while the other component has its maximum above the gas caverns (Fig. 9).

In addition, we inverted the components individually and looked at the component time series of those scatterers that display the strongest magnitude of the components (see Fig. 10). Here, we found that both shows a behavior very similar to the InSAR time series in Fig. 6. which were manually picked to contain only one signal contribution, while the respective other component shows almost no contribution in these scatterers.

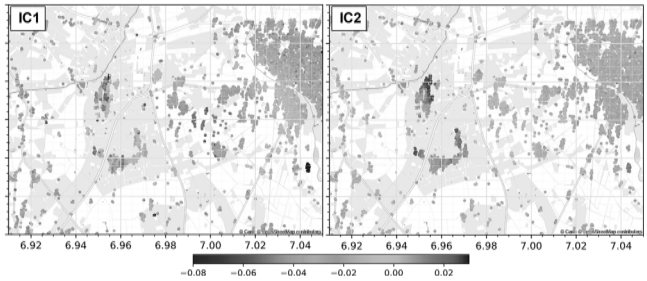

Fig. 9 Results of two ICs of the descending track. The first IC displays its absolute maximum in the center of the cavern field, while the second component only shows up in scatterers in the fen area

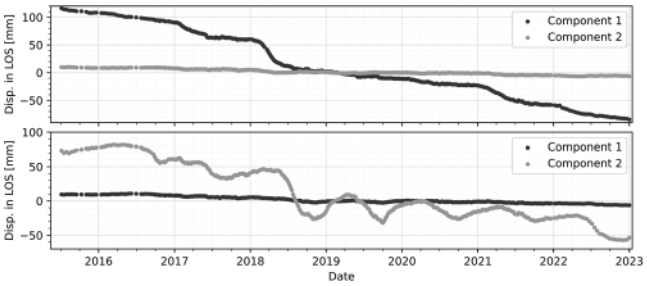

Fig. 10 Component time series from two independent components from the descending track. (**a**) At the maximum of the second component, in the center area of the gas caverns, (**b**) at the maximum of the first component, in the northern fen area

4.3 Parameter Space Search and Fit

The distribution of p_{pres} and p_{fen} in the now denser number of scatterers shows high values above the gas caverns with slowly declining values outward, and high values above the fen, with defined edges between high and low parameter values at the edges of the fen, respectively (see Fig. 11). Their maximum total displacement is 40 mm and 60 mm, respectively. However, p_{lin} shows less clearly distributed values and even displays high values outside of the cavern field. Displacement rates reach up to 50 mm/year in the center of the cavern field, but also for individual scatterers outside.

5 Discussion

5.1 IC Relation to Gas Cavern Filling Levels

Our component time series show very strong similarity with the original time series of the scatterers which we identified as being mostly caused by either the fen or the pressure-related displacements. The spatial distribution and the temporal behavior of the independent components support this observation. Therefore, we can confidently assign IC1 to describing gas cavern behavior and IC2 to the ground water-related displacement. We prove this claim by comparing the time series of IC1 with the filling levels of the gas caverns of Epe in the observation time (see Fig. 12).

For this purpose, we determined the mean filling level of Epe by compiling filling data of all providers (AGSI 2023) and accounted for how many gas caverns are used by each provider. We observe the cyclic signal throughout the component time series having stronger magnitudes where the filling levels were lower (better visible in Fig. 6). This is especially distinct in early 2018, where due to a cold winter, the filling levels dropped down to only 20% resulting in very low pressure inside the caverns and a strong negative displacement of about 5 cm in the component time series. The visible time delay between the emptying of the caverns and the surface response is caused by the viscoelasticity of the salt body in which the caverns lie, as modeled by Even et al. (2020, 2022). As the component time series is dominated by a strong negative trend, a removal of the fitted trend would presumably result in a similar model curve as

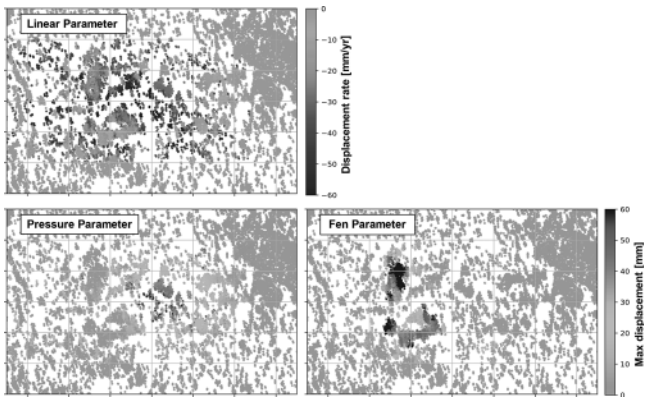

Fig. 11 Fitted parameters in the second InSAR time series result for the track of the ascending orbit. The linear parameter is displayed in mm/year, the pressure and fen parameter as maximum total displacement in mm

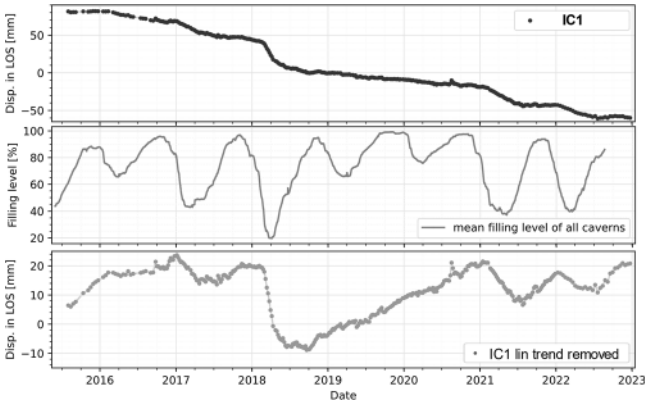

Fig. 12 Displacement time series of IC1 in LOS of the ascending track in the center of the gas caverns (top), component time series of mean filling levels of the gas caverns (source: AGSI 2023) (middle), and trend removed displacement time series of IC1 (bottom)

the filling levels. We find however, that this assumption is only approximately true for the timespans between 2015–2018 and 2021–2023 but does not hold for the years from 2018 to 2021 as displayed in Fig. 12 bottom).

We conclude that the cavern convergence and therefore the resulting subsidence vary with different years, presumably depending on the level of depletion of the caverns in the year. To check this hypothesis, we perform a simple orbit combination (as described in Wright et al. 2004) for one scatterer of both tracks. With this we obtain the vertical displacements in one scatterer of the component time series. We disregard the north component due to lack of sufficient view geometries, being aware that this leads to errors in the estimated vertical displacements. Subsequently, we determined the dates in every year, where the gas caverns reached their highest filling level and added 90 days to account for the delayed surface response described in Sect. 2.2. We then calculate annual linear trends between the displacements at those points in time (see Fig. 13). Subtraction of these trends from the IC1 component time series yields a much better fit with the filling levels (see Fig. 14). The delayed surface response can also be seen clearly now.

Residual discrepancies between the curves can have many causes, such as the influence of the disregarded north displacement component during orbit combination, or the differing depletion levels between different providers and the position of the scatterer regarding to caverns of these providers. Additionally, as described in Liu et al. (2019), the relation between cavern depletion and convergence is even more complex and depends on additional parameters like temperature. And again, the surface response to this process is also more intricate. It will be the subject of future research if the convergence caused subsidence can be sufficiently approximated by an annual linear trend or if we will have to develop a more complex model. However, ICA seems to be able to extract cavern-related displacements sufficiently. Since cavern convergence and cavern pressure are not independent from each other, it is reasonable that ICA cannot separate their effects in surface displacement. Also, in our case, ICA cannot differentiate between gas cavern signals of different providers, which is albeit probably rather related to the close proximity of these caverns to each other and only small differences in filling levels between the providers. Such differences in surface response are too small to be detected with InSAR.

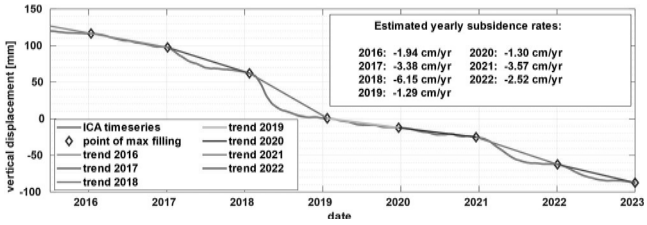

Fig. 13 Component time series of vertical displacements, derived from IC1 in the center of the subsidence bowl and estimated trends between the points of maximum cavern filling of each year shifted by 90 days (as described in Even et al. 2020) to consider for the viscoelasticity of the salt

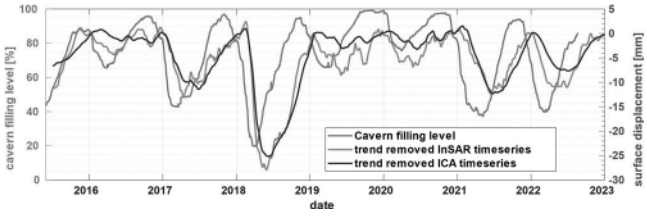

Fig. 14 Vertical displacement curve of original InSAR and IC1 component time series when a annually varying linear trend is removed together with a time series of the mean of the cavern filling levels of all companies

5.2 IC Relation to Groundwater Levels

A similar comparison as in Sect. 4.1 can be made with IC2 and its assumed ground water level relation. We compare component time series of IC2 at the point of its maximum with groundwater measurements (GWM) located near these scatterers. The irregular, yet seasonal shape of the water levels is also visible in the component time series of IC2 (see Fig. 15). After removing a linear trend from the curve, this relation becomes even more clear, proving that IC2 indeed describes the surface displacement related to groundwater changes, which primarily occurs in the fen.

We see that, again between 2018 and 2021, the curve of the trend-removed graph seems to match the GWM a bit less, similar to what we observed for IC1. This indicates that this area may also be affected by yearly varying trends, even though not as prominently as the area above gas caverns. However, it is less likely that these trends are actually caused

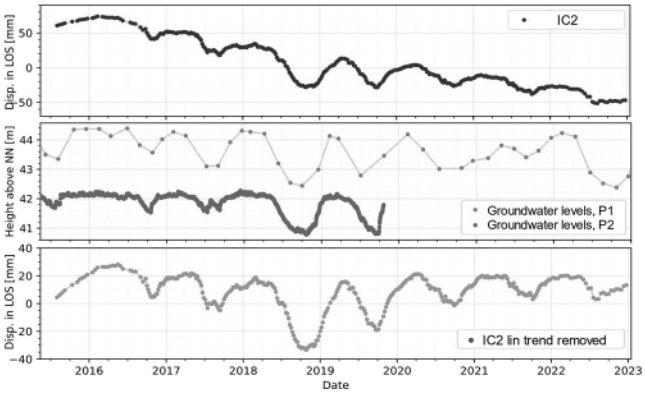

Fig. 15 Component time series of IC2 of the ascending track in the upper fen (top), time series of groundwater levels at two points in the fen (middle) and trend removed component time series of IC2 (bottom). One of the GWMPs only has bi-monthly (or less) measurements, while the other one has daily measurements, but only continues to late 2019, which is why both were included

by the gas caverns, as they are mostly too far away to affect all scatterers in the fen. Rather we presume that these subsidence trends are a combination of the (assumed) linear trends caused by convergence of liquid filled caverns and subsidence that occurs due to the ongoing drying of the fen.

5.3 Parameter Discussion

By utilizing the normalized component time series of the components as displacement models for further time series processing and allowing for DS with lower temporal coherence, we are able to retrieve spatially dense information about the distribution of the signal for the cavern pressure and precipitation-related displacements. The spatial pattern and estimated parameters match with our expectations in terms of magnitude and location of fen boundaries and gas cavern positions and agree with the findings of Even et al. (2020, 2022). However, in case of the linear displacement parameter, the results do not show the expected distribution described by Even et al. (2020, 2022). Even though this parameter seems to be generally higher in the center of the cavern field, there are many scatterers with high values outside of the cavern field. Here we would not expect any relation to cavern convergence. This is presumably related to the inclusion of scatterers with lower temporal coherence. It could also be due to a simple linear trend not being distinct enough to only occur in the subsidence bowl of the cavern field as there is a variety of possible causes for linear trends in scatterers. However, since a linear trend cannot describe displacements caused by cavern convergence for the gas caverns anyway (as shown and discussed in Sect. 4.1), we expect this issue to be resolved when we develop a more complex model for this part of the signal and include it in the parameter estimation instead.

6 Conclusions and Outlook

We used component analysis methods on InSAR time series data of a complex displacement field and showed at the example of the gas cavern field Epe that the retrieved components through ICA can be associated to different source mechanisms. Thus, we show that signal separation in such a complex deformation field is possible, even without using a geophysical source model or a-priori information about the distribution of the different types of displacement.

For other complex displacement fields, where less knowledge about the nature and distribution of the displacement processes is available, this statistical approach of source separation can support extracting and differentiating dominant displacement patterns. Studying this statement in settings with stronger, more complex atmospheric contributions than those occurring in Epe need to be addressed in future studies.

In the case of Epe, the two components identified as the dominant displacements can be assigned to cavern-related and groundwater-related displacements. We were not able to separate displacements originating from cavern convergence and cyclic pressure change with ICA. Trying to fit and remove a linear trend manually proved to not sufficiently describe both displacements. We found that we can better approximate the cavern convergence trends with annual linear trends, depending on the cavern usage in that year. In doing so, we improve upon the parameterized model of the cavern field displacements described in Even et al. (2020, 2022). Our work provides a necessary basis for developing an accurate geophysical source model of the cavern field. This will then help gain a deeper understanding of the processes involved that relate cavern depletion and subsequent convergence to subsequent surface displacement.

Acknowledgments We thank Stefan Meyer from SGW (Salzgewinnungsgesellschaft Westfalen) for providing the GNSS and leveling data, as well as the groundwater measurement data for Epe. We also thank the German Federal Ministry of Economics and Climate Protection (BMWK) for funding this work as part of the SAMUH2 project.

References

Aggregated Gas Storage Inventory (AGSI). https://agsi.gie.eu/#/. Accessed 10 Sept 2023

Comon P (1994) Independent component analysis, a new concept? Signal Process 36:287–314. https://doi.org/10.1016/0165-1684(94)90029-9

Ebmeier SK (2016) Application of independent component analysis to multitemporal InSAR data with volcanic case studies. JGR Solid Earth 121:8970–8986. https://doi.org/10.1109/TGRS.2023.3322595

Even M (2019) Adapting stamps for jointly processing distributed scatterers and persistent scatterers. In: Proceedings of the IGARSS 2019–2019 IEEE international geoscience and remote sensing symposium, Yokohama, Japan, 28 Jul–2 Aug 2019, pp 2046–2049. https://doi.org/10.1109/igarss.2019.8897808

Even M, Westerhaus M, Simon V (2020) Complex surface displacements above the storage cavern field at Epe, NW-Germany, observed by multi-temporal SAR-interferometry. Remote Sens 12:3348. https://doi.org/10.3390/rs12203348

Even M, Westerhaus M, Seidel A (2022) Konvergenz- und druckabhängige Oberflächenverschiebungen über einem Kavernenspeicherfeld in NW-Deutschland, beobachtet mit Methoden der Radarinterferometrie. In: DGMK/ÖGEW Frühjahrstagung 2022 – Geo-energy-systems and subsurface technologies – key elements towards a low carbon world. Deutsche Wissenschaftliche Gesellschaft für Erdöl, Erdgas und Kohle e.V. (DGMK), pp 33–41

Ferretti A, Fumagalli A, Novali F, Prati C, Rocca F, Rucci A (2011) A new algorithm for processing interferometric data-stacks: SqueeSAR. IEEE Trans Geosci Remote Sens 49:3460–3470. https://doi.org/10.1109/TGRS.2011.2124465

Gaddes ME, Hooper A, Bagnardi M et al (2018) Blind signal separation methods for InSAR: the potential to automatically detect and monitor

signals of volcanic deformation. JGR Solid Earth 123. https://doi.org/10.1029/2018JB016210

Hyvärinen A, Oja E (1997) A fast fixed-point algorithm for independent component analysis. Neural Comput 9:1483–1492. https://doi.org/10.1162/neco.1997.9.7.1483

Hyvärinen A, Oja E (2000) Independent component analysis: algorithms and applications. Neural Netw 13:411–430. https://doi.org/10.1016/S0893-6080(00)00026-5

Lin YN, Kositsky AP, Avouac J-P (2010) PCAIM joint inversion of InSAR and ground-based geodetic time series: application to monitoring magmatic inflation beneath the Long Valley Caldera. Geophys Res Lett 37. https://doi.org/10.1029/2010GL045769

Liu H, Zhang M, Liu M, Cao L (2019) Influence of natural gas thermodynamic characteristics on stability of salt cavern gas storage. IOP Conf Ser Earth Environ Sci 227:042021. https://doi.org/10.1088/1755-1315/227/4/042021

Tajduś K, Sroka A, Misa R et al (2021) Surface deformations caused by the convergence of large underground gas storage facilities. Energies 14:402. https://doi.org/10.3390/en14020402

Vajedian S (2020) Incorporating independent component analysis and multi-temporal SAR techniques to retrieve rapid postseismic deformation. ISPRS Ann Photogramm Remote Sens Spatial Inf Sci 3:173–178. https://doi.org/10.5194/isprs-annals-V-3-2020-173-2020

Wang T, Yang C, Yan X et al (2014) Dynamic response of underground gas storage salt cavern under seismic loads. Tunn Undergr Space Technol 43:241–252. https://doi.org/10.1016/j.tust.2014.05.020

Wright TJ, Parsons BE, Lu Z (2004) Toward mapping surface deformation in three dimensions using InSAR. Geophys Res Lett 31:1–5. https://doi.org/10.1029/2003GL018827

Xie P, Wen H, Wang G (2018) An analytical solution of stress distribution around underground gas storage cavern in bedded salt rock. J Renew Sustain Energy 10. https://doi.org/10.1063/1.5004238